Hydration of calcium aluminate cement blended with anhydrite

Gwenn Le Saout, Barbara Lothenbach, Pascal Taquet, Hervé Fryda, Frank Winnefeld

Hydration of calcium aluminate cement blended with anhydrite

Gwenn Le Saoût
Empa, Swiss Federal Laboratories for Materials Science and Technology, Laboratory for Concrete and Construction Chemistry, Dübendorf, Switzerland; presently IMT Mines Alès, Centre des Matériaux de l'École des mines d'Alès (C2MA), Alès, France (corresponding author: gwenn.le-saout@mines-ales.fr) (Orcid:0000-0002-2761-0584)

Barbara Lothenbach
Empa, Swiss Federal Laboratories for Materials Science and Technology, Laboratory for Concrete and Construction Chemistry, Dübendorf, Switzerland

Pascal Taquet
Kerneos Research & Technical Center, Vaulx-Milieu, France

Hervé Fryda
Kerneos Research & Technical Center, Vaulx-Milieu, France

Frank Winnefeld
Empa, Swiss Federal Laboratories for Materials Science and Technology, Laboratory for Concrete and Construction Chemistry, Dübendorf, Switzerland

Calcium aluminate cements (CACs) are used in combination with calcium sulfates as binders in self-levelling mortars. The influence of commercial CAC/anhydrite ratio on the solid phase assemblage and pore solution at water to binder (w/b) ratios of 0·40 and 0·72 was investigated between 1·5 h and 91 d of hydration using a multi-method approach including x-ray diffraction, thermogravimetric analysis and thermodynamic calculations. The reduction of the extent of hydration at the lower w/b ratio can be explained by a lack of water for complete hydration and lack of space. In the system with a CAC/anhydrite weight ratio of 1, ettringite and AH_3 were the main hydration products, whereas in the case of a CAC/anhydrite ratio of 2·3, in addition to ettringite and AH_3, monosulfate was present along with strätlingite and at a later age. In contrast to the thermodynamic modelling results, anhydrite persisted even at low calcium sulfate contents as the precipitation of AH_3 around the anhydrite grains seemed to lead to a chemical blocking.

Introduction

Calcium aluminate cements (CACs) can be used in combination with different calcium sulfate sources as binders of self-levelling mortars for under- and overlayments or screeds. These types of binder, together with special admixtures, make fast drying and rapid strength development possible, as well as shrinkage compensation of the cured mortar (Lutz and Bayer, 2010). The rapid strength development and expansive behaviour are related to the formation of ettringite according to the following reaction (standard cement chemistry notation is used: C = calcium oxide (CaO), A = aluminium oxide (Al_2O_3), F = iron oxide (Fe_2O_3), S = silicon dioxide (SiO_2), $\bar{S}$ = sulfur trioxide (SO_3) and H = water (H_2O)).

I. $\quad 3CA + 3C\bar{S} + 38H \rightarrow C_6A\bar{S}_3H_{32} + 2AH_3$

Monocalcium aluminate CA is the main component of CAC and the sulfate necessary for ettringite formation is provided by blending CAC with calcium sulfates such as anhydrite ($C\bar{S}$), hemihydrate, gypsum or mixes thereof (Glasser *et al.*, 2001). As previously reported in literature (see Bizzozero *et al.* (2014) and references therein), depending on the CA to sulfate ratio, the phase assemblage changes as shown in Figure 1 (derived from thermodynamic calculations of the stable hydrate phases, see section on 'Thermodynamic modelling'). Since ettringite is a water-rich phase, the water demand for complete hydration is considerably higher than for

Portland cement. The highest water demand in the $CA – C\bar{S}$ system corresponds to the maximum ettringite formation (Reaction I). It corresponds to an anhydrite mass fraction of 0·46, and a water to binder (w/b) weight ratio of 0·78 is needed for a complete hydration. In Figure 1, a w/b ratio of 0·80 is used to ensure excess water in the system (the minimum w/b required for complete hydration of CA is indicated on the right-hand axis of the figure). However, materials used for repair or flooring screeds have low w/b ratios in order to achieve high early strengths and are likely to retain much unhydrated binder (Glasser *et al.*, 2001). In commercial CACs, the presence of small amounts of silicon dioxide from impurities in the raw meal may lead to the formation of dicalcium silicate (β-C_2S) and gehlenite (C_2AS) (Odler, 2000). The hydraulic reactivity of β-C_2S changes the phase assemblage and thermodynamic calculations indicate, in the presence of sufficient silicon dioxide, the possible formation of siliceous hydrogrossular ($C_3AS_xH_{6-x}$) and strätlingite (C_2ASH_8), which are more stable than C_3AH_6 (Lothenbach, 2014). Both phases have been observed experimentally in, for example, CAC blended with silica fume or fly ash (Hidalgo Lopez *et al.*, 2008).

In work reported in this paper, the influence of the CAC/anhydrite ratio and the w/b ratio on the kinetics of hydration and phase assemblage of a commercial CAC–anhydrite blend was investigated. A thermodynamic model was used to predict the composition of the solid phases and the results were compared with experimental data.
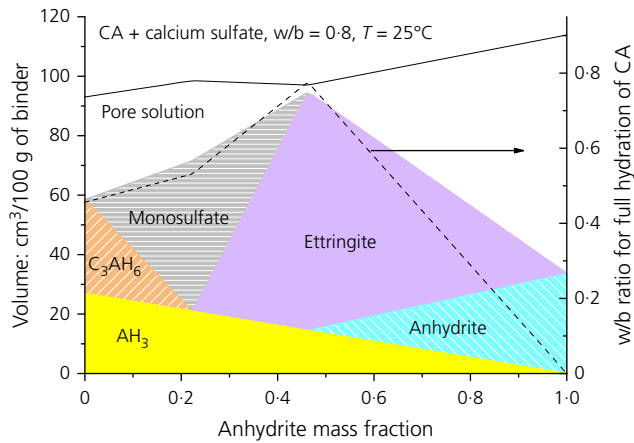
Figure 1. Thermodynamic phase assemblage modelling of the hydration of CA blended with anhydrite as a function of anhydrite weight fraction in the unhydrated blended cement at w/b = 0·80. Volume expressed as cm^3/100 g unhydrated blended cement (left-hand axis). Minimum w/b ratio required for complete hydration of CA is shown on the right-hand axis

Experimental details

Materials

The chemical and mineralogical compositions of the raw materials are listed in Table 1. A commercial CAC (labelled T) and a micronised natural anhydrite (labelled A) were used. Quantitative x-ray diffraction (XRD) was performed by Rietveld analysis (Füllmann *et al.*, 1999). In order to improve the Rietveld analysis of the CAC and especially the detection of minor phases, selective dissolution was carried out according to the protocols proposed by Götz-Neunhoeffer (2003).

The proportions of the raw materials in the four mixes studied are reported in Table 2. Two different anhydrite mass fractions were investigated in order to cover the system (see Figure 1) with ettringite, monosulfate, AH_3 (samples T3 with anhydrite mass fraction of 0·3) and with ettringite, AH_3 (samples T5 with anhydrite mass fraction of 0·5). Two w/b weight ratios were also considered: w/b = 0·72 to ensure excess water in the system (W7) and w/b = 0·40 to retain much anhydrous binder (W4).

Hydration experiments

The pastes were formulated to have a w/b mass ratio of 0·40 (samples labelled T3W4 and T5W4) and 0·72 (samples labelled T3W7 and T5W7). Samples consisting of 100 g of binder and the appropriate amount of water were mixed twice for 90 s according to EN-196-3 (AFNOR, 2009) with a high-shear blender (except for conduction calorimetry).

Conduction calorimetry

A conduction calorimeter (TAM Air, Thermometric AB, Sweden) operating at 20°C was used to determine the hydration heat flow. Admix ampoules described by Wadsö (2005) were used to enable internal mixing, which allows study of the very early hydration reactions.

Analysis of solid phases

Plastic bottles of volume 12 ml were completely filled with the fresh pastes; the bottles were sealed and then stored at 20°C. Prior to thermogravimetric analysis (TGA) and XRD analyses, hydration was stopped after 3, 5, 12 and 18 h and 1, 3, 28 and 91 d by immersing small pieces, each around 2–3 mm^3, for

Table 1. Mineralogical and chemical compositions of the CAC (T) and micronised natural anhydrite (A). Mineralogical composition determined by XRD/Rietveld analysis. Chemical analysis by x-ray fluorescence (except sulfur trioxide) measured with a Leco apparatus

	T: wt%	A: wt%		T:wt%	A: wt%
CA	54·6	—	Sodium oxide (Na_2O)	0·07	0·12
Ferrite (C_4AF)	10·3	—	Magnesium oxide (MgO)	0·47	1·44
Ferrite (C_2AF)	3·0	—	Aluminium oxide (Al_2O_3)	39·75	0·62
Gehlenite (C_2AS)	9·7	—	Silicon dioxide (SiO_2)	4·35	2·33
Perovskite (CT)	6·5	—	Phosphorus pentoxide (P_2O_5)	0·16	0·03
Perovskite (C_3FT)	1·1	—	Sulfur trioxide (SO_3)	0·12	52·07
Magnetite (Fe_3O_4)	6·3	—	Potassium oxide (K_2O)	0·11	0·2
Belite (C_2S)	4·3	—	Calcium oxide (CaO)	36·53	38·61
Phase Q	2·3	—	Titanium dioxide (TiO_2)	1·83	—
Mayenite ($C_{12}A_7$)	1·6	—	Manganese(III) oxide (Mn_2O_3)	0·26	—
Ye'elimite ($C_4A_3\bar{S}$)	0·2	—	Iron(III) oxide (Fe_2O_3)	16·15	0·24
Anhydrite	—	88·1	LOI[b]	0·2	3·7
Gypsum	—	3·6	d_{10}: μm[c]	3·2	2·5
Dolomite	—	6·8	d_{50}: μm	18·0	12·2
Quartz	—	1·5	d_{90}: μm	63·0	45·0
$Na_2O_{soluble}$[a]	0·09	<0·01	Blaine fineness: m^2/kg	3090	4080
$K_2O_{soluble}$[a]	0·03	<0·01	Density: g/cm^3	3·22	2·90

[a]Readily soluble alkalis calculated from concentrations of alkalis measured in the solution after 5 min of agitation at a water to raw materials of 10
[b]Loss on ignition measured until 950°C by TGA
[c]Particle size determined by laser granulometry

Table 2. Contents of CAC (T) and micronised natural anhydrite (A) in the four mixes

	T: g	A: g	Water: g
T5W4	50	50	40
T5W7	50	50	72
T3W4	70	30	40
T3W7	70	30	72

30 min in about 50 ml isopropanol and rinsing twice with diethyl ether. TGA (Mettler Toledo, TGA/SDTA 851e) was performed using about 60 mg of powder at a heating rate of 20°C/min under nitrogen between 30°C and 980°C. The amount of bound water was deduced from the weight losses between 40°C and 550°C.

XRD data were collected using a PANalytical X'Pert Pro MPD diffractometer in a θ–2θ configuration using an incident beam monochromator employing $CuK_{\alpha 1}$ radiation with a fixed divergence slit size of 0·5° and a rotating sample stage. The samples were scanned between 5° and 70° with the X'Celerator detector. The Rietveld analysis was performed with the X'Pert High Score Plus software (version 2.1). The Rietveld refinement of the anhydrous phases and the ICSD (inorganic crystal structure database) codes of the structural data are given in Table 3. Once refinements of the raw materials had been done, the unit cell dimensions and shape parameters of the anhydrous phases were kept constant during refinement of the hydrated pastes. For the hydrated pastes, an external standard calcium fluoride (CaF_2) (G-factor approach) was used to quantify the x-ray amorphous part (Jansen *et al.*, 2011a, 2011b; O'Connor and Raven, 1988; Stabler *et al.*, 2011). The mass attenuation coefficients of the samples were determined by x-ray fluorescence analysis from the data in Table 1, taking into account the amount of bound water determined by TGA. Due to the hydration reactions, water is bound in the hydrates so the total amount of solids increases. In order to correct for this dilution effect, the amount of bound water determined by TGA was deduced, so that the results always refer to the mass of unhydrated binder.

For the microscopic investigations, slices of hydrated samples were cut, immediately immersed in isopropanol for 3 d and then subsequently dried at 40°C for 24 h. They were then impregnated using a low*viscosity epoxy resin and polished down to 0·25 μm using diamond pastes. The obtained polished sections were further coated with carbon (∼5 nm) and examined using a scanning electron microscope (SEM) (Phillips FEG-XL30) coupled with an energy dispersive x-ray spectroscopy (EDX) analyser (EDAX). The EDX point analyses were used to determine the elemental compositions of the hydrate assemblage. The analyses were carried out using an acceleration voltage of 15 kV to ensure a good compromise between spatial resolution and adequate excitation of the FeK_{α} peak. Over 60 points (EDX spots) per sample were analysed.

Analysis of pore solutions

The pore solution analyses were performed only on the samples with the high w/b ratio of 0·72 (T3W7 and T5W7) in order to be able to extract some solution from the samples also at later hydration times. For pore solution extraction, samples consisting of 1 kg binder and 0·72 kg water were mixed according to the EN-196-3 (AFNOR, 2009) standard. The pastes were cast in 500 ml polyethylene bottles, sealed and stored in a thermostatic bath. Pore solutions during the first hours were collected by pressure filtration. At a hydration time of 1 d and beyond, pore fluids were extracted using the steel die method with pressures up to 530 N/mm² (Lothenbach and Winnefeld, 2006). In all cases, the solutions were immediately filtered using 0·45 μm nylon filters. 5 ml aliquots were diluted with 20 ml Milli-Q water. The total concentrations of the element analysed were determined using ion chromatography (Dionex ICS-3000). The pH was measured using a Knick pH meter equipped with a Knick SE 100 electrode calibrated against potassium hydroxide (KOH) solutions of known concentrations.

Thermodynamic modelling

Thermodynamic modelling was used to calculate the effective saturation indices of various hydrate phases that could potentially form in the pastes, using the measured compositions of the pore solution, as well as to model the hydration processes. The Gibbs free energy minimisation software GEMS v.3 was used (see GEMS, 2017; Kulik *et al.*, 2013; Wagner *et al.*, 2012). The thermodynamic data for aqueous species and many solids were taken from the PSI-GEMS thermodynamic database (Hummel *et al.*, 2002), while the solubility products for cement minerals were taken from the Cemdata 14.01 database (see Dilnesa *et al.*, 2014; EMPA, 2017; Lothenbach *et al.*, 2012; Matschei *et al.*, 2007).

The saturation index with respect to a solid is given by log (IAP/K_{s0}), where IAP is the ion activity product, calculated from activities derived from the concentrations determined in the solution, and K_{s0} is the solubility product of the respective solid. A positive saturation index implies oversaturation while a negative value indicates undersaturation with regard to the respective solid. All calculated saturation indices refer to the solubility products of the solids as given by Lothenbach *et al.* (2008, 2012) and Matschei *et al.* (2007). As silicon (Si) concentrations were below detection limit (<0·1 mmol/l), a value of 0·1 mmol/l was assumed in order to calculate the effective saturation indices of strätlingite. The given saturation index of strätlingite represents its upper limit. As the use of saturation indices can be misleading when comparing phases that dissociate into a different number of ions, 'effective' saturation indices were calculated by dividing the saturation indices

Table 3. References of the different phases used for Rietveld analysis

Phase	Formula	Crystal system	ICSD	Reference
Calcium monoaluminate	$CaOAl_2O_3$	Monoclinic	260	Hörkner and Müller-Buschbaum (1976)
Ferrite	Ca_2AlFeO_5	Orthorhombic	9197	Colville and Geller (1971)
Ferrite	$Ca_2Fe_2O_5$	Orthorhombic	98 822	Redhammer *et al.* (2004)
Gehlenite	$Ca_2Al_2SiO_7$	Tetragonal	67 689	Swainson *et al.* (1992)
Perovskite	$CaTiO_3$	Orthorhombic	62 149	Sasaki *et al.* (1987)
Perovskite	$Ca_3TiFe_2O_8$	Orthorhombic	203 100	Rodriguez-Carvajal *et al.* (1989)
Magnetite	Fe_3O_4	Cubic	84 611	Sasaki (1997)
Belite	Ca_2SiO_4	Monoclinic	79 550	Tsurumi *et al.* (1994)
Phase Q	$Ca_{20}Al_{26}Mg_3Si_3O_{68}$	Orthorhombic	26 353	Hanic *et al.* (1980)
Mayenite	$Ca_{12}Al_{14}O_{33}$	Cubic	62 040	Christensen and Lehmann (1984)
Ye'elimite	$Ca_4Al_6O_{12}(SO_4)$	Cubic	9560	Saalfeld and Depmeier (1972)
Anhydrite	$CaSO_4$	Orthorhombic	40 043	Hawthorne and Ferguson (1975)
Gypsum	$CaSO_4\ 2H_2O$	Monoclinic	151 692	De la Torre *et al.* (2004)
Dolomite	$CaMg(CO_3)_2$	Trigonal	31 335	Effenberger *et al.* (1983)
Quartz	SiO_2	Rhombohedral	200 721	Jorgensen (1978)
Kuzelite	$Ca_4Al_2SH_{24}O_{22}$	Trigonal	100 138	Allmann (1977)
Ettringite	$Ca_6Al_2S_3H_{64}O_{50}$	Trigonal	155 395	Götz-Neunhoeffer and Neubauer (2004)

by the number of ions participating in the reactions to form the solids (Lothenbach, 2010).

Thermodynamic modelling of the hydration of the four systems was carried out in a similar manner as described previously, for example for calcium sulfoaluminate cement (Le Saout *et al.*, 2013; Pelletier *et al.*, 2010; Winnefeld and Lothenbach, 2010). By combining an empirical model of the experimental data that describes the dissolution of the clinker phases as a function of time with a thermodynamic equilibrium model, the amount of hydrates formed can be calculated as a function of time.

Results and discussion

Thermodynamic modelling of hydrated cements

Figure 2 shows the thermodynamic modelling of the CAC blended with anhydrite as a function of natural anhydrite mass fraction ratio in the anhydrous blended cement. Complete hydration of the raw materials was assumed apart from for dolomite and quartz in the natural anhydrite and CT, C_3FT, C_2AF, Fe_3O_4 and C_2AS in the CAC as they are known to have low dissolution kinetics at ambient temperature (Pöllmann, 2001). The formation of gibbsite was supressed in all calculations, as well as siliceous hydrogries $Ca_3(Al_xFe_{1-x})_2(SiO_4)_{3-y}(OH)_{4y}$ and gypsum as they were not observed experimentally during the study period. As previously reported and presented later in the paper, the formation of AH_3 with small crystalline size was observed, which differentiates it from well-crystalline gibbsite (Lothenbach *et al.*, 2012).

For a w/b = 0·72, the equilibrium pore solution compositions and phase assemblages are presented in Figures 2(a) and 2(b). The thermodynamic modelling showed, between an anhydrite

mass fraction of 0 and about 0·2, a pore solution in equilibrium with C_3AH_6, monosulfate, strätlingite, AH_3 and FH. At a mass fraction of anhydrite ≥0·2, C_3AH_6 was no longer stable while ettringite became thermodynamically stable; the
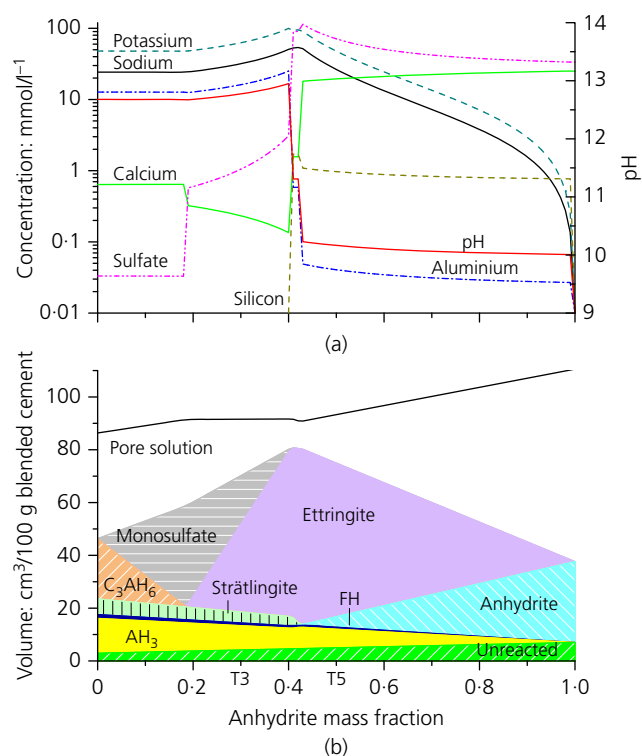

Figure 2. Thermodynamic modelling of the hydration of CAC blended with anhydrite as a function of the anhydrite mass fraction in the unhydrated blended cement. Pore solution (w/b = 0·72) (a) and phase assemblage modelling (b) at w/b = 0·72. Volume expressed as cm³/100 g unhydrated blended cement
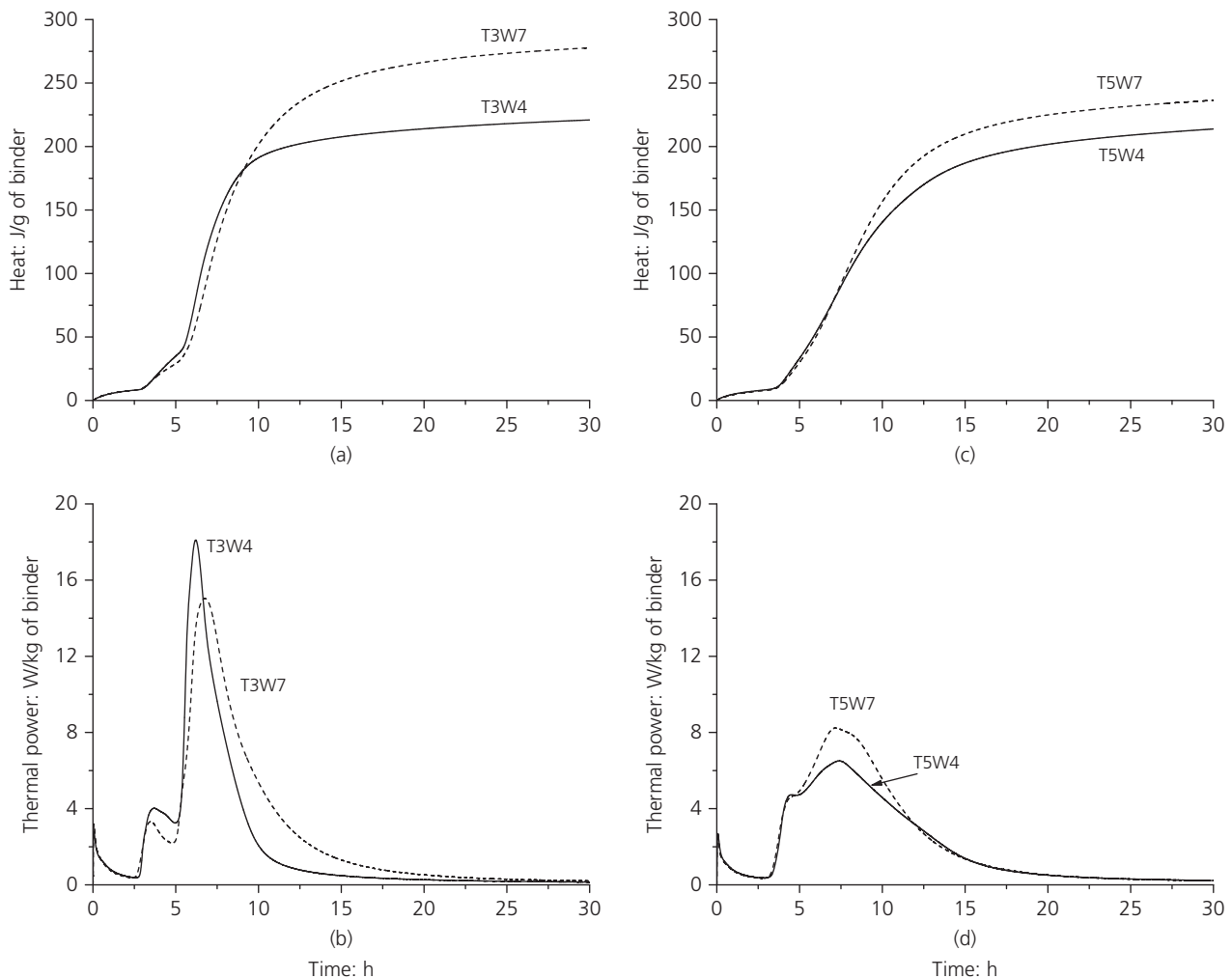
Figure 3. Cumulative heat of cement pastes ((a) and (c)) and heat flow development ((b) and (d)) between 0 and 30 h

concentration of sulfate increased. Another threshold occurred at an anhydrite mass fraction of about 0·4 where strätlingite and monosulfate were not stable anymore and the solution was saturated with respect to anhydrite. The concentrations of calcium, sulfate and silicon increased strongly while aluminium concentrations and pH decreased. Two systems on either side of the threshold at an anhydrite mass fraction of 0·4 were investigated: 0·3 (T3) and 0·5 (T5) with w/b ratios of 0·40 and 0·72. Based on the model, at a w/b ratio of 0·40, a lack of water for full hydration for an anhydrite mass fraction between 0·2 and 0·65 is expected.

Hydration kinetics

Calorimetric measurements of the four mixes with different w/b ratios are shown in Figure 3. The initial period (0–0·5 h) was found to be similar in all systems but the heat observed in this period was certainly influenced by the heat introduced by external mixing (Wadsö *et al.*, 2016). This initial period was

followed by a short induction period of about 2·5 h. During the first 8 h, the heat generated over time was very similar in all systems. A slight increase in the acceleration of hydration in the W4 system was more pronounced for the T3 samples. This can be explained by the decrease in w/b ratio leading to an acceleration of early hydration. A reduction in water is expected to lead to a higher pH in the pore solution, which causes faster dissolution of the clinker phases, as has also been observed in the case of Portland cement (Danielson, 1962). As indicated by the cumulative heat curves after 8 h, a decrease in w/b ratio led to a reduction of the extent of hydration. This can be explained by a lack of water for hydration and/or the filling of space by hydrates, which limits further hydration as observed in blended Portland cement (Berodier and Scrivener, 2015; Glasser *et al.*, 2001). The heat generated in the T3 and T7 systems was different in origin: in T5 it was mainly due to the formation of ettringite and in T3 to ettringite and sulfate–AFm. In the thermal power curves

shown in Figure 3, the first peak appeared in all systems at about 5 h followed by an intense peak in the T3 system and a less intense peak in the T5 system, corresponding to the dissolution of cement phases and the precipitation of hydrates. Continuous in situ XRD measurements with hydration time may be helpful in future studies to determine the assignments of these peaks in more detail, as proposed by Jansen *et al.* (2012).

X-ray diffraction and thermogravimetric analysis

Figure 4 shows experimental diffraction patterns for samples T3 and T5 with a w/b ratio of 0·72. In the T5W7 system (Figure 4(b)), the CA phase reacted quickly and was fully consumed after 12 h (see the diffraction peak at about 30°). The anhydrite started to react significantly at 5 h. After 1 d, hydration slowed down, leaving some unreacted anhydrite in the system (see the (021) diffraction peak at about 31·4°). As CA and anhydrite dissolved, the formation of ettringite as
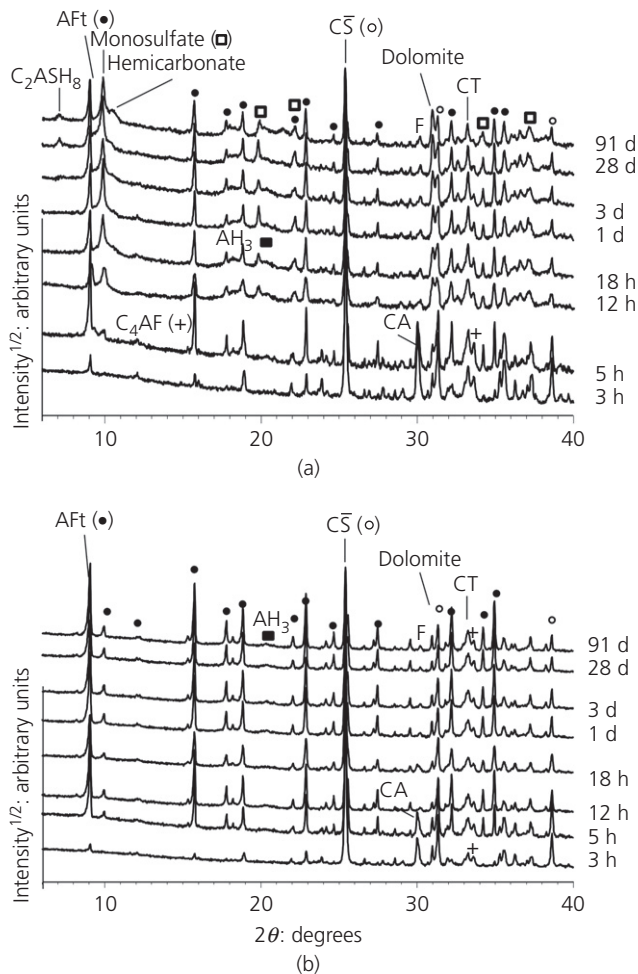
the main hydration product was observed. Some broad reflections of AH_3 were also detected but, as previously reported (Gosselin *et al.*, 2010), AH_3 is not well crystallised and is

Figure 4. Diffraction patterns of (a) T3W7 and (b) T5W7 between 6 and 40°, CuK$_\alpha$
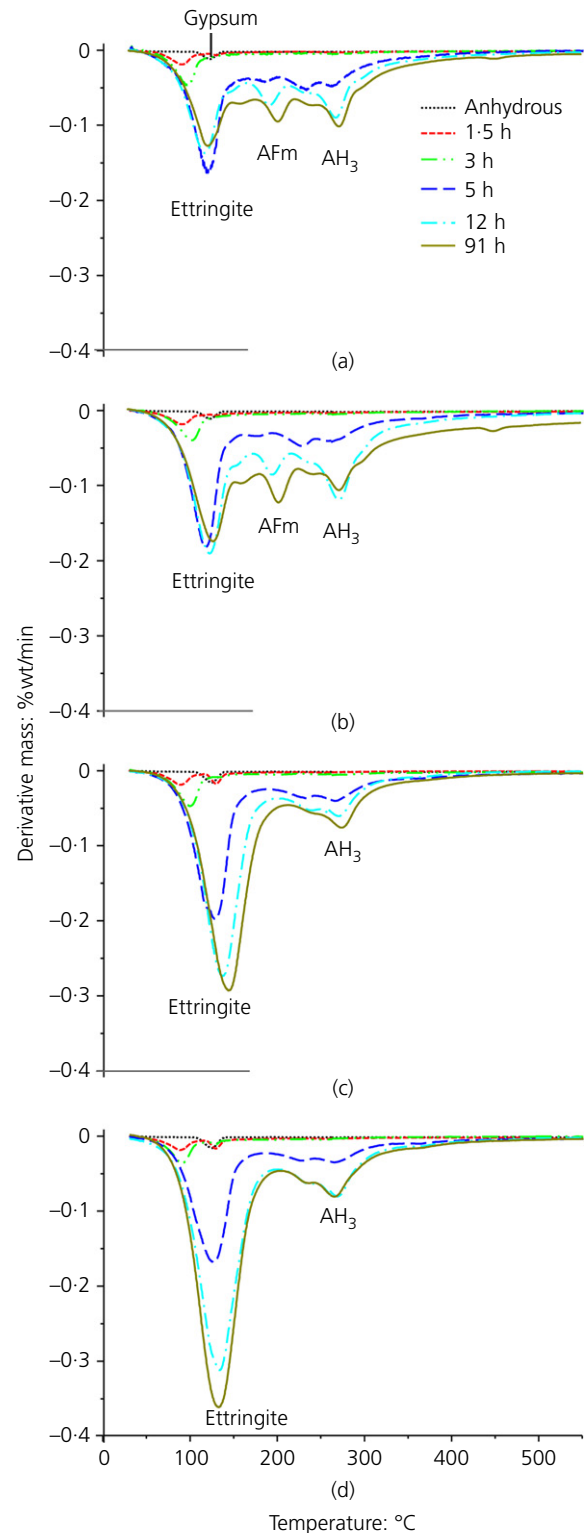

Figure 5. Differential TGA data for (a) T3W4, (b) T3W7, (c) T5W4 and (d) T5W7 pastes

difficult to characterise using XRD. TGA is more appropriate to follow this phase.

The differential TGA curves for T5W7 are presented in Figure 5(d) and the assignments are based on the work of Lothenbach *et al*. (2015). Ettringite was already detected after 1·5 h and its quantity increased with time, as hydration proceeded. As for the ettringite, the amount of aluminium hydroxide ($Al(OH)_3$) increased rapidly until 12 h.

In T5W7, the CA phase reacted with anhydrite to form ettringite and aluminium hydroxide according to Reaction I. The T5W4 system was similar to T5W7 but the decreased w/b ratio led to a reduction of the extent of hydration of CA and anhydrite. According to the thermodynamic calculations (Figure 2), a w/b ratio of 0·54 is needed for complete hydration. As shown by differential TGA (Figure 5(c)), the amount of ettringite in T5W4 was much less than in T5W7 due to a reduction of the extent of reaction of CA and anhydrite as insufficient water was available. XRD results (not shown) showed that, in T5W4, the dissolution of CA and anhydrite slowed down strongly after 12 h and beyond.

In comparison with the T5 system, XRD patterns (Figure 4(a)) of the T3W7 sample also include some reflections of AFm phases: monosulfate and hemicarbonate. From 3 d on, strätlingite (C_2ASH_8) was present in the hydrate assemblage.
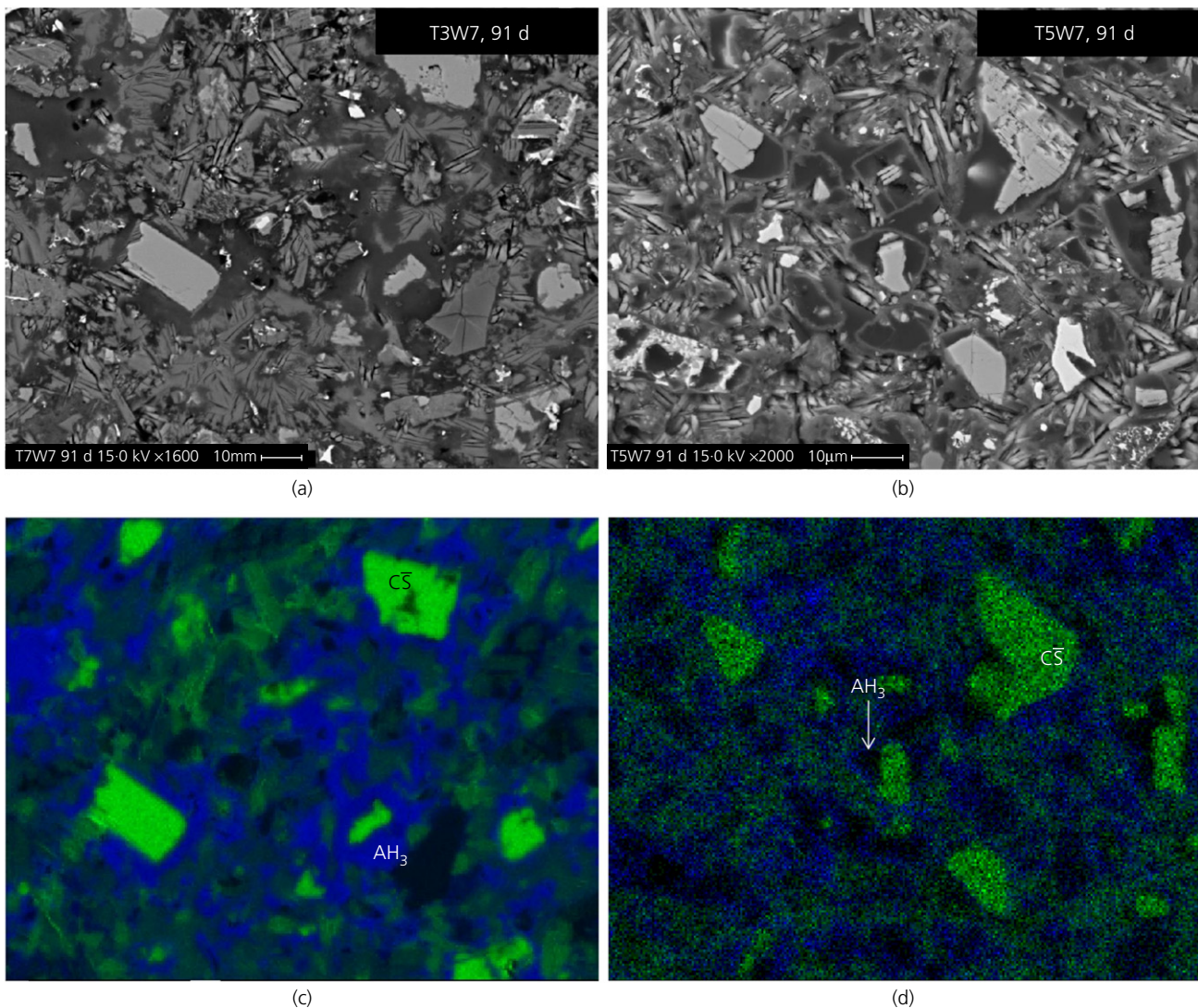

Figure 6. Backscattered images of (a) T3W7 and (b) T5W7 pastes hydrated at 91 d. Element mapping is shown in (c) and (d): sulfur (green) and aluminium (blue). A full-colour version of this figure can be found on the ICE Virtual Library (www.icevirtuallibrary.com)

The persistence of anhydrite in T3W7 was not expected according to thermodynamic modelling (Figure 2). This point will be discussed later with regard to the SEM results. In the differential TGA data shown in Figure 5(b), the peak at about 200°C can be assigned to AFm phase(s). Decomposition of the AFm phases in hydrated ordinary Portland cement usually presents a distinct endotherm between 185°C and 200°C (Lothenbach *et al*., 2015) but it is often not possible to distinguish the different AFm phases (De Weerdt *et al*., 2011). Due to small amount and peak overlaps, it was not possible to follow the thermal dehydration of strätlingite that should occur between 100°C and 210°C (Kuzel, 1976). The differential weight losses associated with ettringite and AH_3 strongly increased between 3 and 5 h. At 5 h, the weight loss due to ettringite remained constant or slightly decreased with time whereas AH_3 continued to increase and a peak associated with the presence of AFm phases appeared at 12 h. Upon further hydration, the weight losses associated with AFm and AH_3 slightly increased with time. The T3W4 system was similar to T3W7 but the decrease in w/b ratio led to a reduction of the extent of hydration and the presence of higher amounts of unreacted CA and anhydrite in the system (according to thermodynamic calculations a w/b ratio of at least 0·50 is needed for complete hydration). The peaks associated with minor phases (C_2S, phase Q, $C_{12}A_7$, ye'elimite and gypsum) were not observed after 3 h, but were difficult to follow due to strong overlapping and the small amount involved. It was also noted that the C_4AF phase seemed to react in the T7 system but not in T5 up to 91 d.

Backscattered electron images (SEM)

Backscattered electron images of the polished surfaces of the T3W7 and T5W7 samples hydrated for 91 d (Figure 6) show the presence of anhydrite. The presence of anhydrite at 91 d in T3W7 and no clear evidence of further dissolution at later ages (similar XRD patterns at 28 and 91 d) seem in contradiction with the thermodynamic modelling (Figure 2(b)). The SEM images revealed that anhydrite grains were embedded in a matrix consisting of AH_3. The rims of AH_3 seem to be larger in T3W7 than in T5W7. As suggested by Bayoux *et al*. (1990), the precipitation of alumina gel around anhydrite grains may lead to chemical blocking due to local interactions at the anhydrite/AH_3 interface and this explains why anhydrite does not fully dissolve. This is confirmed by the thermodynamic modelling, which indicated that the calcium sulfate/AH_3 combination is thermodynamically stable as long as no additional calcium oxide is available. Thus, calcium sulfate becomes chemically unstable and reacts only if the calcium sulfate can interact with solution in contact with CA or AFm phases.

A plot of sulfur/aluminium atomic ratios against calcium/aluminium atomic ratios from the EDX analyses of the hydrated paste (Figure 7), confirms the phase assemblage observed by XRD and TGA. In the T5 system, mainly AH_3 and ettringite are present, whereas in the T3 system the
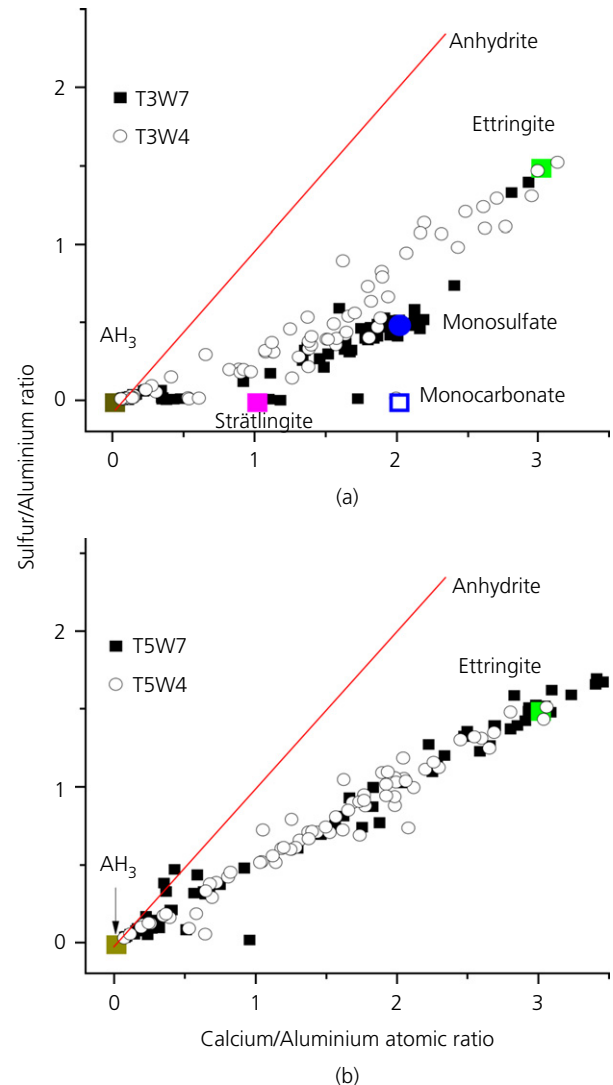

Figure 7. Sulfur/aluminium atomic ratio plotted against calcium/aluminium atomic ratio for individual x-ray microanalyses of the matrix of cement pastes at 91 d

hydrate assemblage consists of a mixture of AH_3, monosulfate and ettringite.

Pore solution

Measured concentrations

Pore solution analysis (Table 4) was performed only on the samples with the high w/b ratio (W7 samples) in order to be able to extract some solution from the samples. As shown by the previous methods of analysis, the main reaction started at around 1·5 h and thus the main variation in the concentration could be observed between 1·5 and 5 h. During this period, the concentrations of potassium, sodium and sulfate increased in the T5W7 sample whereas aluminium decreased and calcium remained constant. The observed increase in alkali

Table 4. Measured total concentrations in the pore solutions gained from T3W7 and T5W7

Time	Sodium: mmol/l	Potassium: mmol/l	Calcium: mmol/l	Aluminium: mmol/l	Sulfate: mmol/l	OH⁻: mmol/l[a]	pH	Bound water[b]
T3W7								
1·5 h	6·1	1·7	15·5	4·6	13·6	1·1	11·0	1·3
3 h	6·2	2·0	10·4	11·4	3·0	1·4	11·1	2·7
5 h	20·5	19·9	2·3	6·7	13·5	5·9	11·7	14·9
8 h	22·5	20·7	3·2	5·8	19·7	4·0	11·5	24·2
12 h	23·9	22·6	2·1	5·9	19·7	5·0	11·6	24·4
18 h	24·4	22·6	1·1	7·7	15·7	7·9	11·8	24·2
1 d	23·4	19·9	0·9	7·0	13·1	8·4	11·8	25·7
3 d	30·8	27·1	0·8	7·2	18·2	13·7	12·0	26·2
7 d	30·2	24·9	0·5	6·3	16·6	13·7	12·0	26·9
28 d	30·9	24·8	0·7	9·7	9·1	25·1	12·3	27·9
T5W7								
1·5 h	10	2	19·3	4·2	18·5	1·0	10·9	1·4
3 h	11	2	12·9	7·5	9·8	1·0	10·9	2·1
5 h	23	13	9·6	2·0	22·5	0·9	10·9	13·4
8 h	27	16	11·3	0·1	28·7	0·7	10·7	26·7
12 h	30	18	12·7	0·4	33·2	0·4	10·5	26·4
18 h	30	18	12·7	0·5	33·9	0·5	10·6	27·2
1 d	28	16	13·5	0·4	32·6	1·1	10·9	28·6
3 d	31	18	16·3	0·1	37·9	0·7	10·8	29·1
7 d	31	16	18·3	<0·1	39·2	0·4	10·5	30·6
28 d	34	17	19·8	<0·1	41·9	0·3	10·3	31·2

[a]Values for OH⁻ refer to the free concentrations and are calculated from GEMS. The measured concentrations of silicon were below the detection limit of 0·1 mM
[b]Bound water content expressed in grams per 100 g of dry binder determined from TGA measurements

and sulfate concentrations may be due to the decrease in pore solution volume as mixing water was consumed by the different hydration products (see bound water content deduced by TGA measurements in Table 4). The decrease in aluminium concentrations coincided roughly with the precipitation of ettringite from the XRD patterns (Figure 4). Afterwards, the pore solution equilibrated with ettringite and anhydrite. The situation was different in the T3W7 system – no decrease in aluminium concentration but a decrease in calcium concentration. The sulfate concentrations were significantly lower, indicating that the pore solution was no longer in equilibrium with ettringite and anhydrite as in T5W7 but with AH_3–AFm–ettringite. This difference was predicted well by the thermodynamic modelling (Figure 2(a)).

Effective saturation indices

The calculation of saturation indices from the concentrations measured in the pore solutions offers the possibility of independently assessing which solid phases may form from a thermodynamic point of view. In T5W7 (Figure 8(b)), the calculated effective saturation indices with respect to ettringite were relatively high, which agrees with the precipitation of ettringite observed by TGA and XRD. The pore solutions were slightly undersaturated at the beginning with respect to anhydrite and slightly oversaturated with respect to microcrystalline AH_3, in agreement with the TGA and XRD results. However, after a few days, the solutions were undersaturated with respect to AH_3, indicating that the AH_3 dissolved under

prolonged hydration. The dissolution of AH_3 was not clearly observed by XRD and TGA but the kinetics of dissolution may be very slow. Initially, the solutions were also slightly saturated with respect to AFm phases (monosulfate and monocarbonate) and strätlingite, indicating that these phases could potentially form, but were not observed experimentally.

The saturation indices calculated for the system T3W7 (Figure 8(a)) were very different from those for T5W7. Initially, the pore solutions were strongly oversaturated with respect to AH_3, indicating that AH_3 could potentially form. However, experimentally, XRD and TGA indicated that no or very little AH_3 was formed in this system initially (before 1·5 h). After 1·5 h, the pore solutions were still oversaturated with AH_3 and slightly oversaturated with respect to ettringite and strätlingite. The saturation indices indicate that all these phases could potentially form upon prolonged hydration. Experimentally, ettringite was observed within the first few hours whereas strätlingite was only observed at about 3 d. The pore solution was also in equilibrium with AFm phases (monosulfate, monocarbonate) as in T5W7 but, in this case, AFm phases were clearly detected by XRD and TGA. An important difference between the two systems is the strong undersaturation of the pore solution with respect to anhydrite in the case of T3W7. This is in apparent contradiction to the XRD data, which showed that anhydrite was still present in the system at a later age. As discussed earlier, the presence of
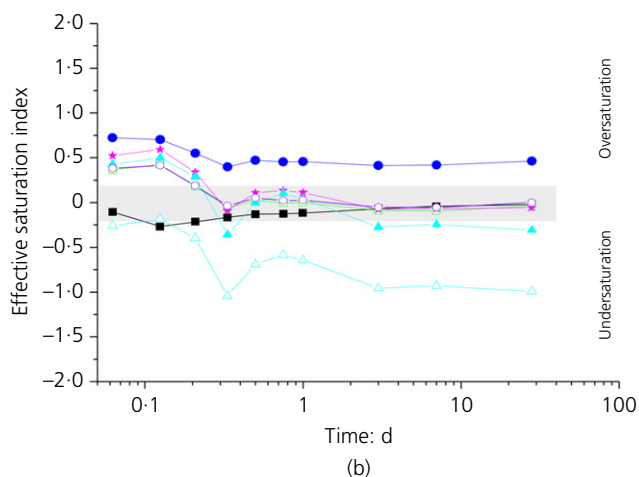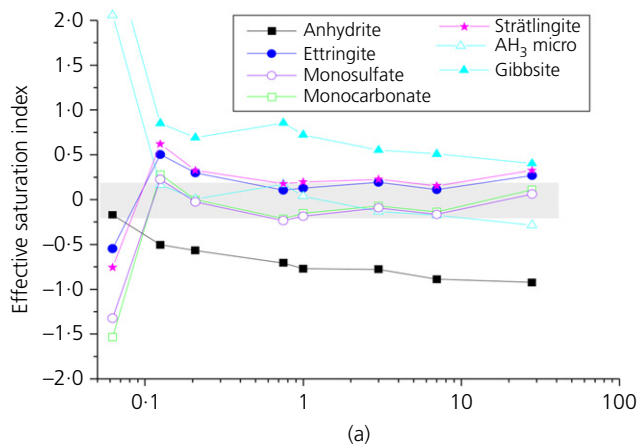
Figure 8. Effective saturation indices of anhydrite, ettringite, AFm phases (monosulfate, monocarbonate), strätlingite and AH_3 micro of hydrated pastes (a) T3W7 and (b) T5W7 as a function of time. The shadowed area indicates saturation

Figure 9. Amount of CA used as input in the thermodynamic model (a) and ettringite (b) deduced by XRD/Rietveld analysis as a function of hydration time. Lines refer to the results of thermodynamic modelling

AH_3 around the anhydrite particle, as observed by SEM, impeded further dissolution of anhydrite.

Thermodynamic modelling of the hydration process

Kinetic input in the thermodynamic model

By combining experimental data of the dissolution of the clinker phases as a function of time with a thermodynamic equilibrium model that assumes equilibrium between the solution and the hydrates, the hydrates formed can be calculated as a function of time. The calculated degree of dissolution of the CA and anhydrite phases based on Rietveld XRD data was fitted by a decaying exponential function after 2·5 h. (Figure 9). In order to take into account the partial dissolution of anhydrite in the system, based on XRD data, for the T3 and T5 systems, hydration degrees of anhydrite of about 65 and 60 wt% respectively were chosen; this led to a good estimation of the amount of ettringite at 91 d using thermodynamic modelling (Figure 9(b)). The conversion of anhydrite to gypsum was also prevented as the experimental data did not
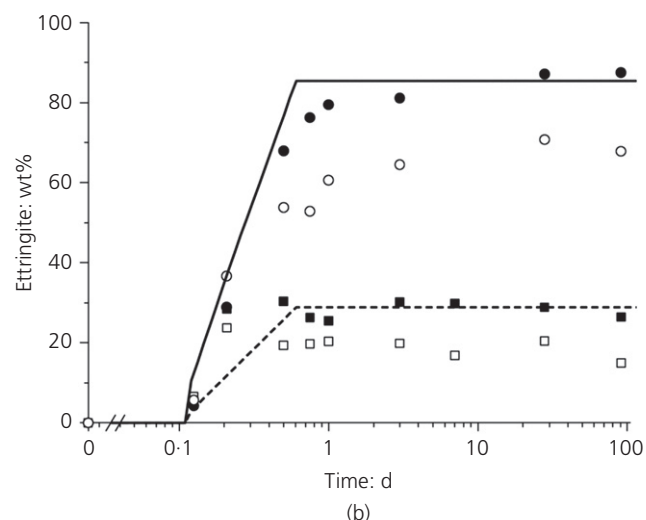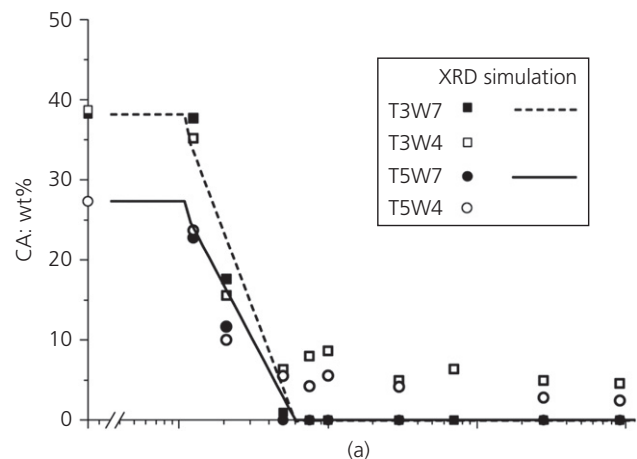
show the occurrence of secondary gypsum, although thermodynamically it was expected.

The unreacted phases in Figure 10 refer to CT, C_3FT, Fe_3O_4, C_2AF, dolomite, quartz and C_2AS. The other phases (C_2S, phase Q, $C_{12}A_7$, ye'elimite and gypsum) were assumed to react after 2·5 h as the peaks were not observed by XRD although their small amounts and peak overlaps did not permit their kinetics to be followed. Based on Rietveld XRD data, it was also assumed that C_4AF did not react in T5 and around 40% reacted in T3.

Development of the hydrate assemblage

Thermodynamic modelling of the two systems is shown in Figure 10. In the T5W7 system, the modelling indicates that different hydrates were formed upon dissolution of the
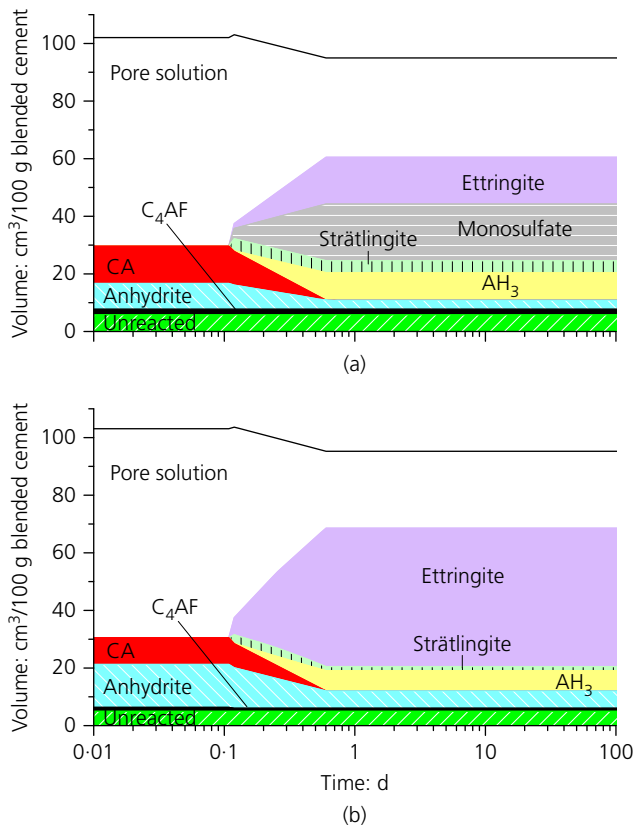
Figure 10. Modelled changes during the hydration of (a) T3W7 and (b) T5W7 as a function of time. Volume expressed as cm³/100 g of unhydrated blended cement. Phases with a volume below 1 cm³ (C_2S, phase Q, $C_{12}A_7$, ye'elimite and gypsum) are not shown in the figure, for clarity

anhydrous phase; initially, mainly ettringite and AH_3. When the sulfates were consumed, the amount of ettringite and AH_3 in the system did not change any further. A small amount of strätlingite was predicted; this was not be detected by XRD and TGA, probably because its quantity was below the detection limit.

In the T3W7 system, the thermodynamic model predicts that as CA is reacting, ettringite, monosulfate and AH_3 precipitate; this was observed by TGA and XRD (Figures 4 and 5). In agreement with the XRD data, strätlingite is predicted at later ages. The amount of ettringite deduced by XRD was in the same range as the calculated quantities (Figure 9(b)). However, the presence of ill-crystallised phases such as AFm and AH_3 were considered part of the x-ray amorphous content and did not permit a quantitative comparison with the modelling to validate the control files.

Conclusion

The aim of this study was to characterise, quantify and model the hydration of commercial CAC blended with anhydrite at

different w/b ratios. The phase assemblage was found to depend strongly on the CAC/anhydrite ratio. In the T5 system (50 wt% of anhydrite, 50 wt% CAC), the phase assemblage was relatively simple with the formation of ettringite and AH_3 phases. In the T3 system (30 wt% of anhydrite, 70 wt% CAC), less ettringite was formed as less calcium sulfate was available. In addition to ettringite and AH_3, monosulfate was present. At later ages, the presence of strätlingite and hemicarbonate was observed. Based on the experimentally observed hydration degrees of CA and anhydrite, the thermodynamic model predicted the hydrate assemblage well. In contrast to the modelling, anhydrite persisted even at low calcium sulfate contents, as the precipitation of AH_3 around anhydrite grains seems to have led to a chemical blocking. A reduction in the extent of hydration was observed at the lower w/b ratio. This can be explained by two factors – a lack of sufficient water for complete hydration and a reduction in the availability of space.

REFERENCES

AFNOR (Association Française de Normalisation) (2009) NF EN 196-3+A1: 2009. Methods of testing cement, Part 3: Determination of setting times and soundness. AFNOR, La Plaine Saint-Denis, France.

Allmann R (1977) Refinement of the hybrid layer structure [Ca₂Al(OH)₈]⁺ [1/2 SO₄ 3H₂O]⁻. *Neues Jahrbuch für Mineralogie* **1977(3)**: 136–144.

Bayoux JP, Bonin A, Marcdargent S and Verschaeve M (1990) Study of the hydration properties of aluminous cement and calcium sulphate mixes. In *Proceedings of the International Symposium on Calcium Aluminate Cement* (Mangabhai RJ (ed.)). E & FN Spon, London, UK, pp. 320–334.

Berodier E and Scrivener KL (2015) Evolution of pore structure in blended systems. *Cement and Concrete Research* **73**: 25–35, https://doi.org/10.1016/j.cemconres.2015.02.025.

Bizzozero J, Gosselin C and Scrivener KL (2014) Expansion mechanisms in calcium aluminate and sulfoaluminate systems with calcium sulfate. *Cement and Concrete Research* **56**: 190–202, https://doi.org/10.1016/j.cemconres.2013.11.011.

Christensen AN and Lehmann MS (1984) Neutron powder diffraction profile refinement studies on Ca₁₁.₃Al₁₄O₃₂.₃ and CaClO(D₀.₈₈H₀.₁₂). *Journal of Solid State Chemistry* **51(2)**: 196–204.

Colville AA and Geller S (1971) The crystal structure of brownmillerite, Ca₂FeAlO₅. *Acta Crystallographica Section B* **27(12)**: 2311–2315.

Danielson UH (1962) Heat of hydration of cement as affected by water–cement ratio. In *Proceedings of the 4th International Symposium on the Chemistry of Cement* (Carlson ET, Steinour HH, Newman ES and Catton MD (eds)). National Bureau of Standards, Washington, DC, USA, Monograph 43, vol. I, paper IV-S7, pp. 519–526.

De la Torre AG, Lopez-Olmo MG, Alvarez-Rua C, Garcia-Granda S and Aranda MAG (2004) Structure and microstructure of gypsum and its relevance to Rietveld quantitative phase analyses. *Powder Diffraction* **19(3)**: 240–246.

De Weerdt K, Ben Haha M, Le Saout G *et al.* (2011) Hydration mechanisms of ternary Portland cements containing limestone powder and fly ash. *Cement and Concrete Research* **41(3)**: 279–291.

Dilnesa BZ, Lothenbach B, Renaudin G, Wichser A and Kulik D (2014) Synthesis and characterization of hydrogarnet $Ca_3(Al_xFe_{1-x})_2(SiO_4)_y(OH)_{4(3-y)}$. *Cement and Concrete Research* **59**: 96–111, https://doi.org/10.1016/j.cemconres.2014.02.001.

Effenberger H, Kirfel A and Will G (1983) Untersuchungen zur Elektronendichteverteilung im Dolomit $CaMg(CO_3)_2$. *Tschermaks Mineralogische und Petrographische Mitteilungen* **31(1–2)**: 151–164 (in German).

EMPA (2017) http://www.empa.ch/web/s308/cemdata (accessed 05/07/2017).

Füllmann T, Walenta G, Bier T, Espinosa B and Scrivener K (1999) Quantitative Rietveld phase analysis of calcium aluminate cements. *World Cement Research* June 1999: 1–6.

GEMS (GEM Software) (2017) http://gems.web.psi.ch (accessed 05/07/2017).

Glasser FP, Zhang L and Zhou Q (2001) Reactions of aluminate cements with calcium sulphate. In *Proceedings of the International Conference on Calcium Aluminate Cement* (Mangabhai RJ and Glasser FP (eds)). IOM Communications, London, UK, pp. 551–564.

Gosselin C, Gallucci E and Scrivener K (2010) Influence of self-heating and Li_2SO_4 addition on the microstructural development of calcium aluminate cement. *Cement and Concrete Research* **40(10)**: 1555–1570.

Götz-Neunhoeffer F (2003) Quantitative phase analysis of various Fe-rich calcium aluminate cement clinkers by selective dissolution and XRPD. In *Proceedings of the 11th International Congress on the Chemistry of Cement* (Grieve G and Owens G (eds)). Document Transformation Technologies, Gauteng, South Africa, pp. 125–134 (CD-ROM).

Götz-Neunhoeffer F and Neubauer J (2004) Refined ettringite $(Ca_6Al_2(SO_4)_3(OH)_{12} \cdot 26H_2O)$ structure for quantitative X-ray diffraction analysis. *Powder Diffraction* **21(1)**: 4–11.

Hanic F, Handlovic M and Kapralik I (1980) The structure of a quaternary phase $Ca_{20}Al_{32-2x}Mg_xSi_xO_{68}$. *Acta Crystallographica Section B* **36(12)**: 2863–2869.

Hawthorne FC and Ferguson RB (1975) Anhydrous sulphates. II. Refinement of the crystal structure of anhydrite. *The Canadian Mineralogist* **13(3)**: 289–292.

Hidalgo Lopez A, Garcia Calvo JL, Garcia Olmo J, Petit S and Cruz Alonso M (2008) Microstructural evolution of calcium aluminate cements hydration with silica fume and fly ash additions by scanning electron microscopy, and mid and near-infrared spectroscopy. *Journal of the American Ceram Society* **91(4)**: 1258–1265.

Hörkner W and Müller-Buschbaum HK (1976) Zur kristallstruktur von $CaAl_2O_4$. *Journal of Inorganic and Nuclear Chemistry* **38(5)**: 983–984 (in German).

Hummel W, Berner U, Curti E, Pearson FJ and Thoenen T (2002) *Nagra/PSI Chemical Thermodynamic Data Base 01/01*. Universal Publishers, Parkland, FL, USA.

Jansen D, Götz-Neunhoeffer F and Neubauer J (2011a) A remastered external standard method applied to the quantification of early OPC hydration. *Cement and Concrete Research* **41(6)**: 602–608.

Jansen D, Stabler C, Götz-Neunhoeffer F, Dittrich S and Neubauer J (2011b) Does ordinary Portland cement contain amorphous phase? A quantitative study using an external standard method. *Powder Diffraction* **26(1)**: 31–38.

Jansen D, Goetz-Neunhoeffer F, Lothenbach B and Neubauer J (2012) The early hydration of Ordinary Portland Cement (OPC): an approach comparing measured heat flow with calculated heat flow from QXRD. *Cement and Concrete Research* **42(1)**: 134–138.

Jorgensen JD (1978) Compression mechanisms in alpha-quartz structures -SiO_2 and GeO_2. *Journal of Applied Physics* **49(11)**: 5473–5478.

Kulik DA, Wagner T, Dmytrieva SV *et al.* (2013) GEM-Selektor geochemical modeling package: revised algorithm and GEMS3K numerical kernel for coupled simulation codes. *Computers & Geosciences* **17(1)**: 1–24.

Kuzel HJ (1976) Crystallographic data and thermal decomposition of synthetic gehlenite hydrate $2CaO \cdot Al_2O_3 \cdot SiO_2 \cdot 8H_2O$. *Neues Jahrbuch für Mineralogie* **1976(7)**: 319–325.

Le Saout G, Lothenbach B, Hori A, Higuchi T and Winnefeld F (2013) Hydration of Portland cement with additions of calcium sulfoaluminates. *Cement and Concrete Research* **43**: 81–94, https://doi.org/10.1016/j.cemconres.2012.10.011.

Lothenbach B (2010) Thermodynamic equilibrium calculations in cementitious systems. *Materials and Structures* **43(10)**: 1413–1433.

Lothenbach B (2014) Thermodynamic modelling of effect of time and silica on the conversion process. In *Proceedings of the International Conference on Calcium Aluminates* (Fentiman C, Mangabhai RJ and Scrivener K (eds)). IHS BRE Press, Watford, UK, pp. 153–164.

Lothenbach B and Winnefeld F (2006) Thermodynamic modelling of the hydration of Portland cement. *Cement and Concrete Research* **36(2)**: 209–226.

Lothenbach B, Matschei T, Möschner G and Glasser FP (2008) Thermodynamic modelling of the effect of temperature on the hydration and porosity of Portland cement. *Cement and Concrete Research* **38(1)**: 1–18.

Lothenbach B, Pelletier-Chaignat L and Winnefeld F (2012) Stability in the system $CaO–Al_2O_3–H_2O$. *Cement and Concrete Research* **42(12)**: 1621–1634.

Lothenbach B, Durdziński PT and De Weerdt K (2015) Thermogravimetric analysis. In *A Practical Guide to Microstructural Analysis of Cementitious Materials* (Scrivener K, Snellings R and Lothenbach B (eds)). CRC Press, Boca Raton, FL, USA, pp. 177–211.

Lutz H and Bayer R (2010) Dry mortars. In *Ullmann's Encyclopedia of Industrial Chemistry* (Elvers B (ed.)). Wiley-VCH, Weinheim, Germany, pp. 541–579.

Matschei T, Lothenbach B and Glasser FP (2007) Thermodynamic properties of Portland cement hydrates in the system $CaO–Al_2O_3–SiO_2–CaSO_4–CaCO_3–H_2O$. *Cement and Concrete Research* **37(9)**: 1379–1410.

O'Connor BH and Raven MD (1988) Application of the Rietveld refinement procedure in assaying powdered mixtures. *Powder Diffraction* **3(1)**: 2–6.

Odler I (2000) *Special Inorganic Cements: Modern Concrete Technology 8*. E & FN Spon, London, UK.

Pelletier L, Winnefeld F and Lothenbach B (2010) The ternary system Portland cement-calcium sulphoaluminate clinker–anhydrite: hydration mechanism and mortar properties. *Cement & Concrete Composites* **32(7)**: 497–507.

Pöllmann H (2001) Mineralogy and crystal chemistry of calcium aluminate cement. In *Proceedings of the International Conference on Calcium Aluminate Cement* (Mangabhai RJ and Glasser FP (eds)). IOM Communications, London, UK, pp. 79–119.

Redhammer GJ, Tippelt G, Roth G and Amthauer G (2004) Structural variations in the brownmillerite series $Ca_2(Fe, Al)O_5$: single-crystal X-ray diffraction at 25°C and high temperature X-ray powder diffraction (25°C<T<1000°C). *American Mineralogist* **89(2–3)**: 405–420.

Rodriguez-Carvajal J, Vallet-Regi M and Calbet JG (1989) Perovskite threefold superlattices: a structure determination of the $A_3M_3O_8$ phase. *Materials Research Bulletin* **24(4)**: 423–430.

Saalfeld H and Depmeier W (1972) Silicon-free compounds with sodalite structure. *Crystal Research and Technology* **7(1–3)**: 229–233.

Sasaki S (1997) Radial distribution of electron density in magnetite, Fe_3O_4. *Acta Crystallographica Section B* **53(5)**: 762–766.

Sasaki S, Prewitt CT and Bass JD (1987) Orthorhombic perovskite $CaTiO_3$ and $CdTiO_3$: structure and space group. *Acta Crystallographica* **C43(9)**: 1668–1674.

Stabler C, Götz-Neunhoeffer F, Neubauer J, Estival J and Taquet P (2011) In-situ investigation of calcium aluminate cement-based dry-mix mortars with improved shelf life properties. In *Tagung Bauchemie GDCh Monograph* (Schmidt-Döhl F and Deckelmann G (eds)). GDCh, Frankfurt am Main, Germany, vol. 44, pp. 68–73.

Swainson IP, Dove MT, Schmahl WW and Putnis A (1992) Neutron powder diffraction study of the akermanite–gehlenite solid solution series. *Physics and Chemistry of Minerals* **19(3)**: 185–195.

Tsurumi T, Hirano Y, Kato H, Kamiya T and Daimon M (1994) Crystal structure and hydration of belite. *Ceramic Transactions* **40**: 19–25.

Wadsö L (2005) Applications of an eight-channel isothermal conduction calorimeter for cement hydration studies. *Cement International* **3(5)**: 94–101.

Wadsö L, Winnefeld F, Riding K and Sandberg P (2016) Calorimetry. In *A Practical Guide to Microstructural Analysis of Cementitious Materials* (Scrivener K, Snellings R and Lothenbach B (eds)). CRC Press, Boca Raton, FL, USA, pp. 37–74.

Wagner T, Kulik DA, Hingerl FF and Dmytrieva SV (2012) GEM-Selektor geochemical modeling package: TSolMod library and data interface for multicomponent phase models. *Canadian Mineralogist* **50(5)**: 1173–1195.

Winnefeld F and Lothenbach B (2010) Hydration of calcium sulfoaluminate cements – experimental findings and thermodynamic modeling. *Cement and Concrete Research* **40(8)**: 1239–1247.